Zipeng Guo
Department of Industrial and Systems Engineering,
University at Buffalo,
The State University of New York,
Buffalo, NY 14260
e-mail: zipenggu@buffalo.edu

Lu An
Department of Mechanical and Aerospace Engineering,
University at Buffalo,
The State University of New York,
Buffalo, NY 14260
e-mail: luan@buffalo.edu

Sushil Lakshmanan
Department of Industrial and Systems Engineering,
University at Buffalo,
The State University of New York,
Buffalo, NY 14260
e-mail: sushilla@buffalo.edu

Jason N. Armstrong
Department of Mechanical and Aerospace Engineering,
University at Buffalo,
The State University of New York,
Buffalo, NY 14260
e-mail: jna4@buffalo.edu

Shenqiang Ren
Department of Mechanical and Aerospace Engineering,
University at Buffalo,
The State University of New York,
Buffalo, NY 14260;
Department of Chemistry,
University at Buffalo,
The State University of New York,
Buffalo, NY 14260
e-mail: shenren@buffalo.edu

Chi Zhou[1]
Department of Industrial and Systems Engineering,
University at Buffalo,
The State University of New York,
Buffalo, NY 14260
e-mail: chizhou@buffalo.edu

Additive Manufacturing of Porous Ceramics With Foaming Agent

The macro-porous ceramics has promising durability and thermal insulation performance. As porous ceramics find more and more applications across many industries, a cost-effective and scalable additive manufacturing technique for fabricating macro-porous ceramics is highly desirable. Herein, we reported a facile additive manufacturing approach to fabricate porous ceramics and control the printed porosity. Several printable ceramic inks were prepared, and the foaming agent was added to generate gaseous bubbles in the ink, followed by the direct ink writing and the ambient-pressure and room-temperature drying to create the three-dimensional geometries. A set of experimental studies were performed to optimize the printing quality. The results revealed the optimal process parameters for printing the foamed ceramic ink with a high spatial resolution and fine surface quality. Varying the concentration of the foaming agent enables the controllability of the structural porosity. The maximum porosity can reach 85%, with a crack-free internal porous structure. The tensile tests showed that the printed macro-porous ceramics possessed enhanced durability with the addition of fiber. With a high-fidelity three-dimensional (3D) printing process and the precise controllability of the porosity, we showed that the printed samples exhibited a remarkably low thermal conductivity and durable mechanical strength.
[DOI: 10.1115/1.4051828]

Keywords: additive manufacturing, ceramic aerogel, direct ink writing, macro-porous structure, colloidal ink, foaming agent, electrostatic stabilization

1 Introduction

The additive manufacturing (AM) of porous ceramics has attracted intense attention due to their lightweight structure, high specific surface area, customized geometry, structural aesthetic, and multi-functionalities. These unique merits open up tremendous opportunities in wide-spreading applications, including energy storage [1,2], thermal insulation [3,4], soundproofing [5,6], wearable textiles [7], and tissue engineering [8]. Multiple AM techniques have been explored to fabricate porous ceramics in three-dimensional (3D) geometries; stereolithography (SLA) is capable of producing the most complex ceramic shapes [9,10]. Drop-on-demand inkjet printing is capable of manipulating the hierarchical structures both internally and externally [11]. Owing to the scalability and low cost, extrusion-based direct ink writing (DIW) has been mostly used for three-dimensionally fabricating porous ceramics. The ceramic ink for the printing consists of the ceramic powder, the solvent, and the additive chemicals for tuning the rheological behavior. A highly viscous and non-Newtonian fluid with shear-thinning behavior is most suited for the DIW [12]. The printable ink can be deposited along the pre-defined path by using either the pneumatic pressure or the mechanical forces for the extrusion. The post-processing steps include solvent removal and heat treatments.

[1]Corresponding author.
Manuscript received July 6, 2021; final manuscript received July 8, 2021; published online August 5, 2021. Tech. Editor: Y. Lawrence Yao.

Conventionally, porous ceramics are preferable candidates for thermal insulation purposes. However, when additive manufacturing methods are applied to fabricate porous and lightweight ceramics, several challenges hinder the pathway. The solvent removal process is one of the critical steps for making crack-free porous ceramics. Due to the interfacial tension between the solvent and the ceramic, cracking could easily happen during the drying process. To overcome this issue, Zhao et al. used the supercritical drying method to remove the solvent from the printed silica aerogel [3]. Though effective, the prolonged drying time and the use of large-amount hazardous organic solvent pose challenges for sustainable and large-scale productions. The alternative method to prevent large shrinkage and damage is using freeze-drying. Li et al. [13] printed the water-based gel and froze the sample at −20 °C environment. Then, ice crystals were subsequently sublimed during the freeze-drying process, and the ice-occupied space was left with empty pores, with most of them being open pores. In a previous study [14], we proposed the method of using a surfactant to reduce the interfacial tension and followed by the cost-effective ambient-pressure drying for printing the silica aerogel in 3D geometries. The results showed that by adding the surfactant, no obvious pore collapsing was observed, with the pore size between 100 μm and 250 μm generated. Due to the low equipment cost and time cost, ambient-pressure drying is preferable for scalable productions. The aforementioned approaches prevent the structure from collapsing and create porous internal structures of the printed objects; however, further developments are needed to grant the porous ceramic with enhanced thermal insulation properties. The controllability of the pore size and pore shape is critical for the thermal insulation performance of porous ceramics [15–19]. Due to the limited porosity that can be created from the solvent exchange, researchers have explored strategies to introduce additional pores and form the interconnected macro-pores in the printed porous ceramics. Two routes have mostly been studied: direct foaming and sacrificial templating. Originally, these techniques are widely used in manufacturing bulk ceramics due to their facility in generating multiscale pores, ranging from 0.5 μm to 1 mm. When combined with the DIW technique, it can achieve the customized geometry with the internal porous structure. Muth and coauthors designed the foamed viscoelastic ink by introducing the air bubbles in the ink [20,21]. The foamed alumina ink was printed to lightweight cellular objects, with closed-porous struts. Huang et al. printed the SiOC with a hierarchical porous structure using sacrificial microbeads [22]. The microbeads were embedded in the ceramic ink. After printing, the microbeads were pyrolyzed at high temperatures and thus formed the porous structure. By changing the size of the microbeads, the pore size and the geometry can be precisely controlled. A similar idea was adopted by Chan et al. [23], they used sunflower oil to prepare the emulsion. Minas et al. [24] added octane to the alumina suspension to form the emulsion ink. Sugar was used by Maurath et al. to create millimeter-sized pores in printing the bone scaffold structure [25].

Our previous study showed promising results in printing the silica aerogel in complex 3D geometries, exhibiting a low thermal conductivity of 0.053 W m^{-1} K^{-1}. Following the aforementioned evolution of technical advancements, herein, we reported the generic process parameter study for improving the printing quality of the ceramic, such that the desired macro-porous structure and associated functionalities can be obtained. Figure 1 shows the schematic diagram of the printing process. The silica nanoparticle, silica aerogel, and alumina were used for the study to demonstrate the generality of the proposed approach. The significance and contribution of this work are that we reported the effectiveness of using the foaming agent to print the lightweight macro-porous ceramics. Tuning the foaming agent content allows controlling the porosity of the printed parts. Also, the printing process parameter studies were used to optimize the printing surface quality. With the high process fidelity and structure controllability, we can print macro-porous ceramics in high spatial resolution and dimensional accuracy. As a result, the thermal insulation performance of the printed macro-porous ceramics reached a significantly lower level. The methods are explained in Sec. 2, and the results from the experimental investigations are presented in Sec. 3. An in-depth and comprehensive discussion is detailed in Sec. 4.

2 Methods

2.1 Ink Composition and Preparation. Three types of preformed ceramic powder were used for preparing the printable ink, including synthesized silica aerogel powder from the waterglass-based (sodium silicate) precursor [26], the silicon oxide nanoparticles (SkySpring Nanomaterials, TX), and the alumina powder (INFRAMAT, CT). Polyvinyl alcohol (PVA, MW 9000–10,000, Sigma Aldrich) was mixed with deionized (DI) water at 80 °C, and then, the ceramic powder was added to the solvent at 65 wt% concentration. The fiber (Isofrax 92; UNIFRAX, NY) was added with various ratios to the ceramic fiber (from 10 wt% to 60 wt%) and followed by homogenously mixing for 3 h, at 600 rpm on a magnetic stirring hot plate (Thermo Scientific, Waltham, MA). Hydroxypropyl methylcellulose (HPMC, Sigma-Aldrich, St. Louis, MO) was added to the ink as a viscosity modifier at a concentration of 12 mg/mL of the DI water, followed by 3-h mixing at 150 rpm on the magnetic stirring plate. The ink shear-thinning behavior was obtained after the mixing. The foaming agent cetyltrimethylammonium bromide (CTAB, VWR, Radnor, PA) was added to the ink prior to printing. The concentration varies from 0.05 wt% to 0.30 wt%, depending on the targeted porosity. Vigorously blending

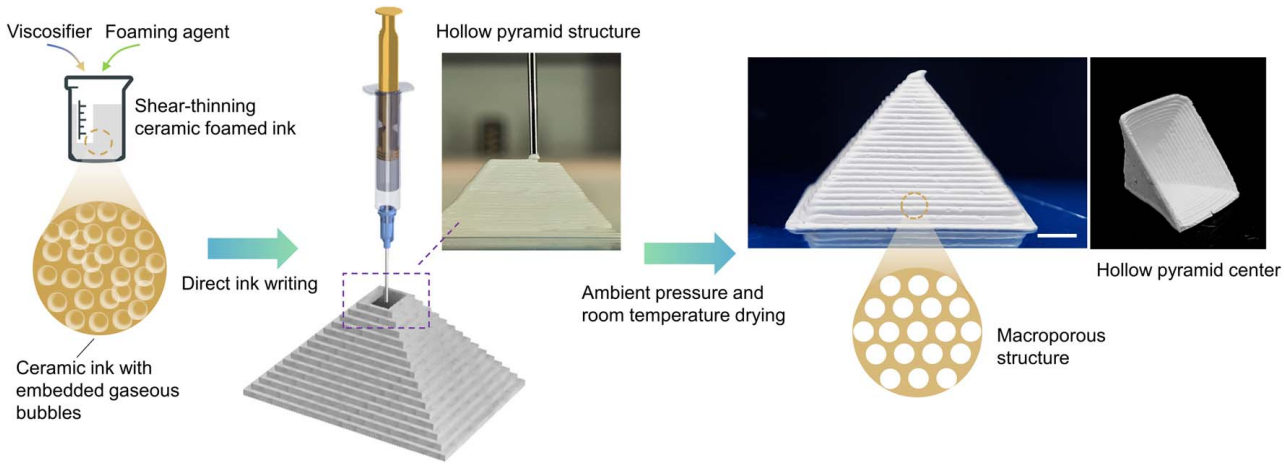

Fig. 1 Schematic diagram of the direct writing of foamed ceramic ink. Scale bar represents 2 mm.

the mixture for 30 min can produce gaseous bubbles inside the ink. Bubbles retain the size and quantity after one week of aging in a closed container.

2.2 Direct Writing of the Foamed Ceramic Ink. A custom-assembled 3D printer was constructed, and two different extrusion configurations were adopted for printing the ceramics. The pneumatic pressure extrusion utilized the air pressure for depositing the ink. An air compressor was used to generated and store the air pressure. The regulator (Nordson EFD, RI) controlled the pressure to extrude the ink. The other configuration used the pneumatic-driven plunger (Nordson EFD, RI). As the pneumatic pressure is exerted on the plunger, a downward mechanical force is generated, which then exerts on the piston of the syringe, and subsequently extruding the ink. The prepared ink was loaded into a 10-mL syringe with a luer-lock nozzle (Nordson EFD, RI) attached to the syringe. Four types of nozzles were tested for investigating the preferable configuration toward printing the parts with the best quality: the plastic-made conical shape nozzle, the metal-made conical shape nozzle, the straight nozzle, and the conical body with straight tip nozzle. All the nozzles have an inner diameter of 0.4 mm. The extruder path and G-code are generated by Slic3r software (slic3r.org). A hollow pyramid computer-aided design (CAD) model was sliced with a layer thickness of 0.3 mm. The hollow pyramid model has a wall thickness of 1 mm, and the center region of the pyramid was empty. The free-standing property of the ceramic ink can be well demonstrated using this model. The hollow pile structure was printed for the layer thickness study, with each pile in one layer. A stainless-steel woven mesh sheet was used as a substrate. The fine meshes on the thin sheet are permeable to air, which prevents the printed sample from cracking caused by non-uniform drying. In addition, the flexible mesh sheet can be easily peeled off from the sample without damaging the bottom surface. The printing results and comparison between different configurations are shown in the Results section.

2.3 Ambient-Pressure and Room-Temperature Drying. The as-printed samples were dried in an ambient-pressure and room-temperature environment. After 6-h drying, the mesh substrate can be easily peeled off from the sample. With additional 6-h drying, the solvent was completely evaporated; consequently, the porous ceramic was obtained. Slightly increasing the drying temperature can further reduce the drying time. With a 60 °C and moisture-maintained environment, the drying process can take 10 h. The printed silica aerogel samples took less time to get fully dried than the silica and alumina powder-based sample because silica aerogel has a much larger surface area than others. However, we used consistent drying conditions across all the printed samples to control the variations.

2.4 Porosity Measurement. The helium gas pycnometer (AccuPyc II 1340, Micrometritics; Norcross, GA) was used to measure the true volume of the printed samples. The particle density was calculated by taking the ratio of the mass to the true volume. With the cubic shape samples, the bulk density was calculated by taking the ratio of the mass to the measured bulk density. Then, the sample porosity was calculated by

$$\text{Porosity} = 1 - \frac{\rho_{\text{Bulk}}}{\rho_{\text{Particle}}}$$

2.5 Thermal Conductivity Measurement. The thermal conductivities were carried out using a custom-built thermal conductivity sensing instrument. The printed samples were placed between two identical plates in a parallel geometry. A heated plate (remain constant at 37 °C) was placed at the top and a cooled plate (remain constant at 30 °C) at the bottom. Heat flux sensors were attached to each plate. The relationship between the heat flux value and the thermal conductivity is given by

$$q = \frac{-\lambda \times \Delta T}{\Delta t}$$

q represents the heat flux value, λ is the thermal conductivity, ΔT is the temperature difference across the sample, and Δt is the thickness of the sample.

2.6 Mechanical Characterization. The uniaxial tensile testing was performed with the testing machine (United Testing Systems, Fullerton, CA). Before the tensile tests, the sample surfaces were milled and polished using sandpaper to smooth the surface to conduct accurate mechanical measurements.

2.7 Microstructural Characterization. The scanning electron microscopy (SEM) was used to reveal the morphology and microstructure of the printed ceramics. The images were taken with the Carl Zeiss AURIGA CrossBeam focused ion beam SEM (White Plains, NY). The sample surfaces were sputter-coated with gold for 40 s at 20-mA current.

3 Results

3.1 Direct Writing of the Foamed Ceramic Ink. Figure 2 shows the four types of nozzles, with the just-extruded filament from the nozzle tip. The nozzles have an inner diameter of 0.4 mm. As can be seen from the printed hollow pyramids, all the samples are free-standing in the designed structure, indicating the ink has suitable rheology conditions for the DIW process. The comparison between the samples reveals that both the straight nozzles can print the uniform layers. Primarily because the velocity of the ink flow can be stabilized within the straight region of the nozzle, the stable extrusion ensures the continuous filament can always stay in a cylindrical shape. Therefore, we can have uniform layers as shown in the figure.

The conical nozzles require a lower level of extrusion pressure; thus, it is widely used for thicker ink printing [27–30]. Since the nozzle shape changes from tail to tip, the ink velocity also varies within the nozzle. Consequently, the filament is not in a cylindrical shape, and the printed ceramic part does not have a delicate surface.

Since the conical body with a straight tip nozzle can print the most detailed features with the ceramic ink, we continued using this type of nozzle (0.5 mm) for the layer thickness study. As shown in Figs. 3(*a*)–(*d*), the hollow piles structures were printed with different layer thicknesses, from 0.35 mm to 0.50 mm. Each pile occupies one single layer. All the printed piles can self-support in the hollow regions. When the layer thickness was equal to the nozzle size (0.5 mm, Fig. 3(*d*)), the piles have the most circular

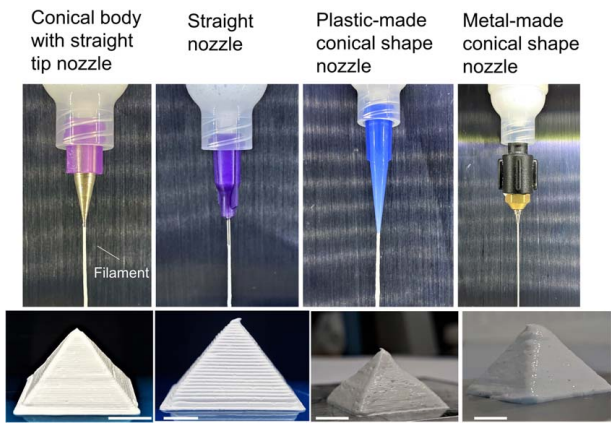

Fig. 2 The nozzle type study. The scale bars represent 5 mm.

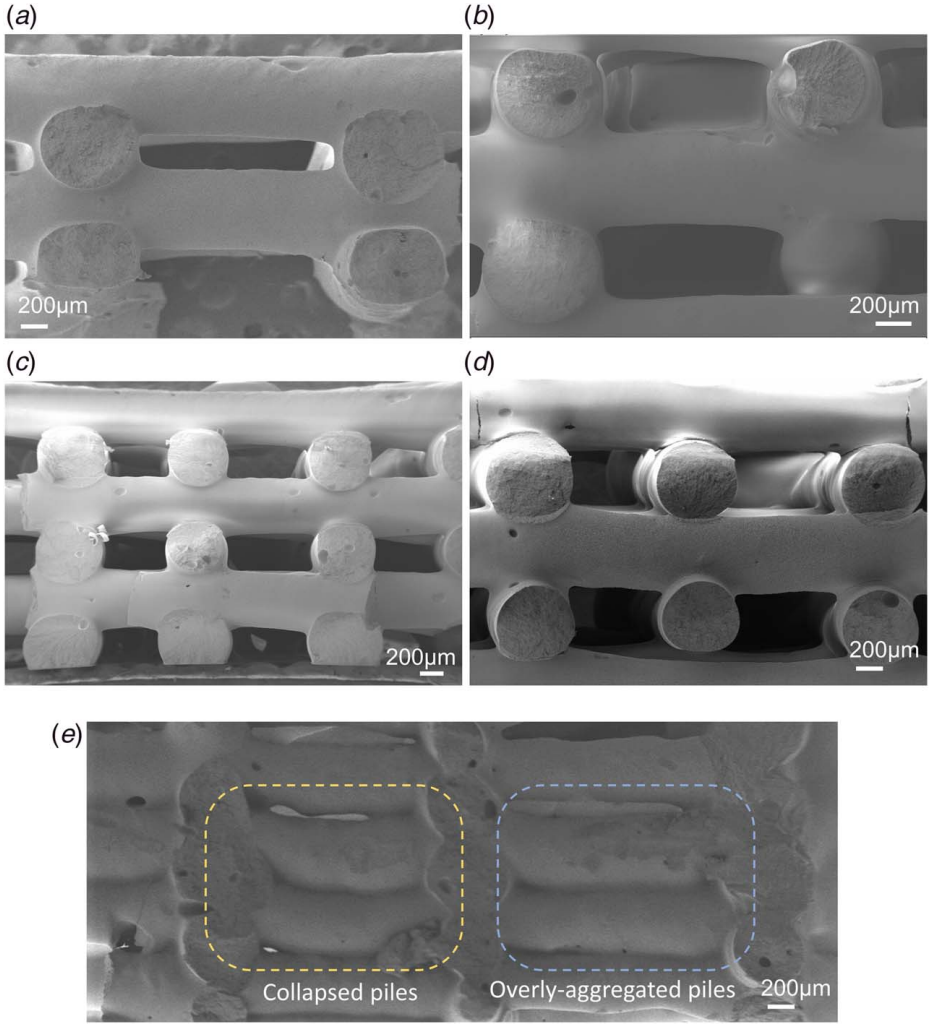

Fig. 3 The printed hollow piles structures for the layer thickness study: (*a*) layer thickness, 0.35 mm; (*b*) 0.40 mm; (c) 0.45 mm; and (*d*) 0.50 mm. (e) The collapsed piles and the overly aggregated piles.

shape. When the layer thickness is less than the nozzle size, each layer of the pile slightly presses down on the lower pile. Therefore, the cross-sectional views of piles are in an elliptical shape. In this context, after pressing down on the previous layer, the contact area between the layers increases and the inter-layer bonding could gain benefits and subsequently ensuring a preferable mechanical strength. In contrast, Fig. 3(*e*) shows the collapsed piles and overly aggerated piles. The individual piles cannot support themselves due to the over-extrusion and insufficient viscosity of the ink [31].

3.2 Macro-Size Porous Structure. The microstructures of the printed ceramics shown in Fig. 4 were characterized with the scanning electron microscope (SEM). The silica aerogel SEM images are shown in Fig. 4(*a*), the size of smaller pores is approximately 50 μm, and the majority are closed pores. Larger size pores range from 100 μm to 150 μm. The zoom-in figure (Fig. 4(*b*)) shows the pores are in regular spherical shapes, which reflects the spherical shape of the gaseous bubbles. The cross section of the alumina sample is shown in Fig. 4(*c*), the pore size is also ranging from 50 μm to 150 μm, and the majority of the pores are closed pores. As shown in Fig. 4(*d*), the shape of the pores is not uniformly spherical. The comparison of the morphology also reveals that the silica aerogels are more porous than the alumina samples.

3.3 Porosity Measurements. Figure 5 shows the porosity measurements of the printed samples. CTAB as the foaming agent was used at different concentrations. The dense sample without CTAB was also printed as the control sample. Contributed by the mesoporous nature, silica aerogel has a 62.6% porosity, even without adding the foaming agent. While with only 0.05 wt% CTAB, a significant increase can be observed in the porosity. As indicated by the dashed curve, samples with 0.25 wt% and higher CTAB concentration approach the plateau of the porosity. The highest porosity is 85.1%, with a CTAB concentration of 0.3 wt%. For the case of silica, the increase in the porosity is more prominent. With the dense sample only having 48% porosity, adding the CTAB (0.3 wt%) can increase the porosity as high as 81%. The alumina samples also demonstrated similar results. In this way, the material cost for producing such porous ceramics can be largely saved.

3.4 Mechanical Characterization. Our previous study presented the mechanical properties of the 3D-printed silica aerogel under compressional stress, it was found by uniformly depositing fiber to the silica aerogel ink, and the printed samples can be reinforced in compression strength [14]. Herein, we printed the silica aerogels in tensile bar shapes with different fiber concentrations and then studied their mechanical behavior under the tensional stress. The Isofix-92 fiber (Unifrax) was added to the ink, at

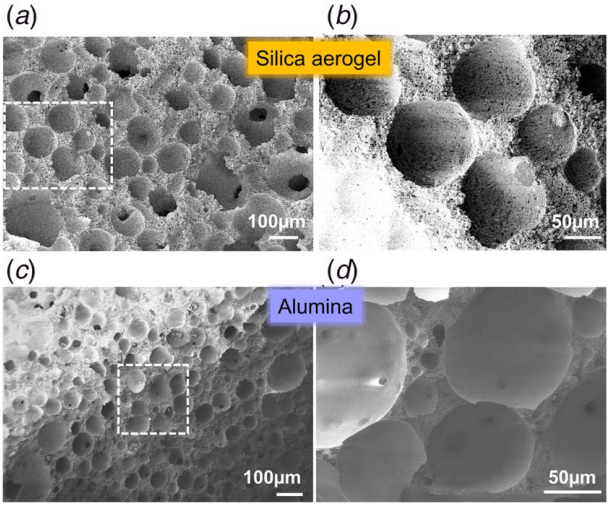

Fig. 4 Macro-porous structure of the printed sample

concentrations of 30 wt%, 40 wt%, 50 wt%, and 60 wt%, respectively. The stress–strain curves are plotted in Fig. 6(*a*), with the increasing fiber concentration, the elastic modulus and the tensile strength are also increased. The elastic modulus and tensile strength are plotted against the fiber concentration in Fig. 6(*b*). With 60 wt% fiber concentration, the printed aerogel sample has an elastic modulus of 119 MPa and tensile strength of 3.52 MPa, with a strain of 6%. The SEM image of the fiber-embedded aerogel sample is shown in Fig. 6(*c*). It shows the planar cross section of the 3D-printed sample, and the fibers are closely embedded in the aerogel.

3.5 Thermal Conductivity Measurements. With all the discoveries on the optimum printing configuration and the porosity controlling results, we printed the silica aerogels to measure the thermal conductivity. In this measurement, we used the straight nozzle (0.5 mm) with a layer thickness of 0.35 mm to print the fine surfaces. A fine finishing surface can guarantee the contact between the sample and the heat flux sensor, such that the results can be accurate and referenceable. The foaming agent was added at different concentrations, from 0.05 wt% to 0.3 wt%. The dense structure without any foaming agent was also printed as the

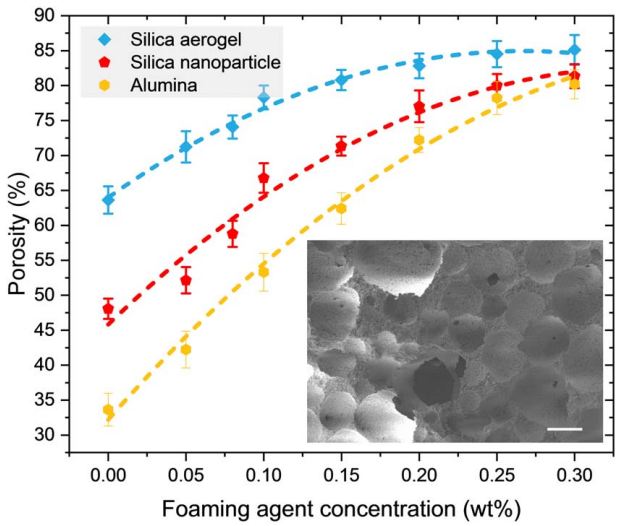

Fig. 5 Porosity measurement of the printed samples. Scale bar represents 50 μm.

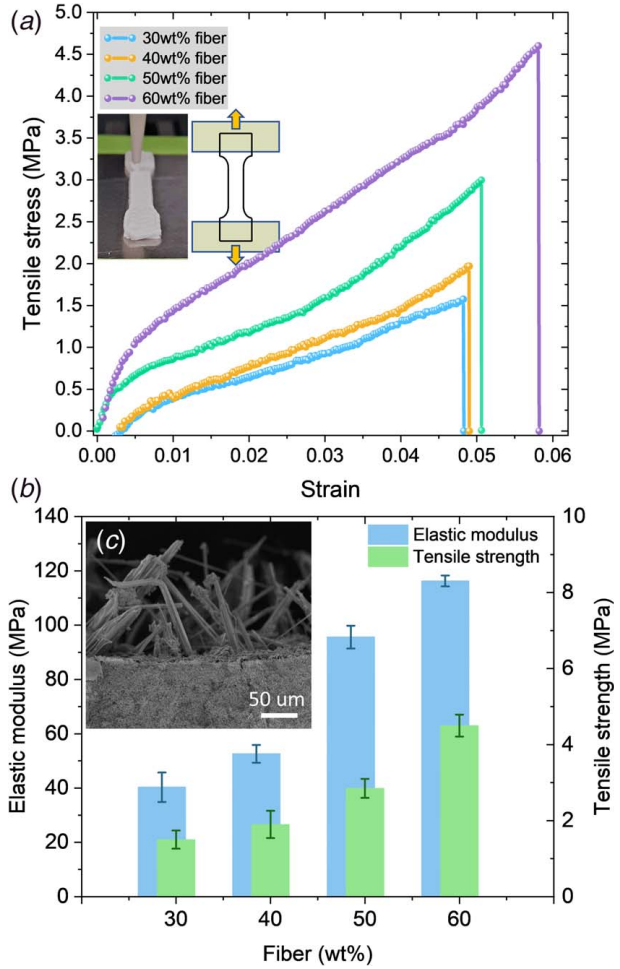

Fig. 6 Mechanical characterization of the printed samples under tensional stress. (*a*) Stress–strain curves of samples with different fiber concentrations. (*b*) The elastic modulus and the tensile strength as the function of fiber concentrations. (*c*) SEM image of the cross-sectional area of the printed tensile bars.

control sample. The dimension of the samples was 30 mm by 30 mm by 4 mm. The thermal conductivity was plotted against the foaming agent concentration in Fig. 7. It can be clearly seen that adding the foaming agent helps to enhance the thermal insulation performance of the printed silica aerogels. The dense samples have a thermal conductivity of 0.082 W m^{-1} K^{-1}, while the 30 wt% foaming agent samples have the lowest thermal conductivity of 0.031 W m^{-1} K^{-1}. With the increasing porosity, more gaseous voids break the continuity of the heat transport pathway, and thus, the thermal conductivity decreases.

4 Discussion

From our previously presented work, we realized that controlling the porosity, pore size, and pore shape is critical for improving the thermal insulation property of the printed macro-porous ceramics. On top of the macro-porous structure, ensuring the printed spatial resolution is the foremost foundation. Targeted on these goals, we performed the printing process parameters studies to find the optimal configuration of the nozzle type with the best corresponding layer thickness so that it helps to improve the printing quality. Furthermore, by studying the effectiveness of the foaming agent for tuning the porosity, the printed macro-porous ceramics can have the designed pore size, distribution, and quantity. As a result, the lowest thermal conductivity reaches 0.031 W m^{-1} K^{-1} for the 3D-printed silica aerogel.

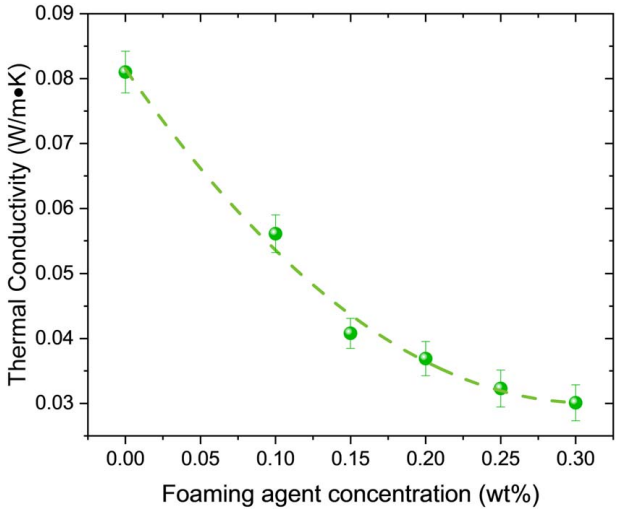

Fig. 7 Thermal conductivity measurement. The measurements were conducted with the printed silica aerogel samples.

Coupled with the direct ink writing is the ambient pressure and temperature drying (APD). Conventionally the APD method has the challenge of maintaining the pore structure and preventing collapsing [32]. Here, contributed by the surfactant-like foaming agent (CTAB), it can reduce the surface tension between the solvent and the ceramic particles. On the other hand, in a ceramic colloidal suspension, the particles can mostly stay stable and against aggregation by the presence of the electrostatic repulsion [33–35]. To introduce the electrostatic repulsion to the ink, a surface charge at the interface between the gas bubbles and the colloidal liquid should be first created. The charged surfaces can repel each other, thus building electrostatic stabilization. The CTAB as a cationic surfactant is positively charged, when contacting with water, they generate the surface-active cations and further creates the surface charge and surface potential [36]. Consequently, abundant gaseous bubbles can be created in the ceramic ink and stay uniformly distributed.

As indicated in Fig. 5, the foaming agent can effectively generate the macro-porous structures. The spherical shape of the pores reflects the original shape of the gaseous bubbles. After drying, the bubbles are gone and left the occupied space with the empty pores. When comparing the pore shape of the silica aerogel and the alumina, it is clear that the silica aerogel sample has a more regular spherical shape, while the alumina sample pores were deformed slightly to an irregular spherical shape. This is because the silica aerogel has a much lower particle density than the alumina; thus, the gaseous bubbles can support themselves in the spherical shape, while the alumina puts more weight on the bubbles, which caused the slight deformation of the spherical shape. By adding the foaming agent, the porosity can be rationally controlled. The maximum porosity can reach as much as 85%, with only 0.3 wt% concentration of the CTAB foaming agent.

On top of the high-porosity and lightweight structure, we also expect the printed sample to have certain stiffness and durability. In the tensional stress study, we investigated the sample printed with fiber at various concentrations. Since the fiber was mixed with the ink, after printing, fiber was closely embedded in the ceramic structure. Also contributed by the additives in the ink recipe, such as the binder (PVA), facilitates the structural integrity reinforcement. When the printed samples were loaded with tensile stress, unlike the conventional brittle ceramics, the ceramic structure cannot withstand much tensional load. While in the case of fiber-embedded samples, a certain portion of the load transfers to the fiber. Due to the elasticity of the fiber, it subsequently absorbs part of the strain energy. This energy-absorbing mechanism leads to a form of pseudo-plasticity, which grants the printed sample higher tensile strength and stiffness. The generality of our proposed macro-porous foaming and the direct ceramic ink writing method was presented with the silica aerogel, the silica nanoparticles, and the alumina. The silica aerogel represents the category of mesoporous ceramic material, and our previous study presents its thermal insulation functionality in 3D-printed geometries. The macro-porous silica and alumina in three-dimensional structures grant them promising high-temperature and harsh environment applications. Owing to the nature of the APD, the cost-effectiveness in time and equipment allows the proposed approach to be scalable toward mass production. Future works can be developed towards creating the hierarchical porous structures in the printed sample by combining the direct foaming method and the sacrificial templating. With a multiscale porous structure, more functionalities such as soundproof, catalyst support, and filtration can be discovered on the 3D-printed ceramics.

5 Conclusions

The approach of 3D printing the macro-porous ceramics with controllable porosity was presented in this paper, with the goal of optimizing the printing fidelity and accordingly reducing the thermal conductivity of the printed samples. The experimental investigation on the process parameters indicated the optimum configuration for printing ceramic ink with fine quality and high fidelity. The porosity of the printed macro-porous ceramics can be controlled by tuning the concentration of the foaming agent. Coupling the fine printing surface quality and the preferred structural porosity allows the printed samples to possess enhanced thermal insulation performance. The possibility of scalable 3D printing of the lightweight macro-porous ceramics with durable strength will prove beneficial for broad applications such as thermal insulation, customized architectures, biomedical components, wastewater treatment, soundproof, and energy storage devices.

Acknowledgment

The authors would like to gratefully acknowledge the support from the U.S. National Science Foundation (NSF) through Grant No. CMMI-1846863 and U.S. Department of Energy (DOE), Office of Energy Efficiency and Renewable Energy through Grant No. DEEE-0008675. We thank Dr. Mark Swihart for the scientific discussions. The fiber sheet was kindly provided to us by Unifrax Inc.

Conflict of Interest

There are no conflicts of interest.

Data Availability Statement

The data sets generated and supporting the findings of this article are obtainable from the corresponding author upon reasonable request. The authors attest that all data for this study are included in the paper. Data provided by a third party are listed in Acknowledgment. No data, models, or code were generated or used for this paper.

References

[1] Wu, Z. S., Winter, A., Chen, L., Sun, Y., Turchanin, A., Feng, X., and Müllen, K., 2012, "Three-Dimensional Nitrogen and Boron Co-doped Graphene for High-Performance All-Solid-State Supercapacitors," Adv. Mater., **24**(37), pp. 5130–5135.
[2] Zhao, J., Zhang, Y., Zhao, X., Wang, R., Xie, J., Yang, C., Wang, J., Zhang, Q., Li, L., Lu, C., and Yao, Y., 2019, "Direct Ink Writing of Adjustable Electrochemical Energy Storage Device With High Gravimetric Energy Densities," Adv. Funct. Mater., **29**(26), p. 1900809.
[3] Zhao, S., Siqueira, G., Drdova, S., Norris, D., Ubert, C., Bonnin, A., Galmarini, S., Ganobjak, M., Pan, Z., and Brunner, S., 2020, "Additive Manufacturing of Silica Aerogels," Nature, **584**(7821), pp. 387–392.

[4] Bertino, M., 2018, "Rapid Fabrication of Hybrid Aerogels and 3D Printed Porous Materials," J. Sol-Gel Sci. Technol., **86**(2), pp. 239–254.
[5] Liu, Z., Zhan, J., Fard, M., and Davy, J. L., 2016, "Acoustic Properties of a Porous Polycarbonate Material Produced by Additive Manufacturing," Mater. Lett., **181**, pp. 296–299.
[6] Cao, L., Fu, Q., Si, Y., Ding, B., and Yu, J., 2018, "Porous Materials for Sound Absorption," Compos. Commun., **10**, pp. 25–35.
[7] An, L., Liang, B., Guo, Z., Wang, J., Li, C., Huang, Y., Hu, Y., Li, Z., Armstrong, J. N., and Zhou, C., 2021, "Wearable Aramid–Ceramic Aerogel Composite for Harsh Environment," Adv. Eng. Mater., **23**(3), p. 2001169.
[8] Du, X., Fu, S., and Zhu, Y., 2018, "3D Printing of Ceramic-Based Scaffolds for Bone Tissue Engineering: An Overview," J. Mater. Chem. B, **6**(27), pp. 4397–4412.
[9] Song, X., Zhang, Z., Chen, Z., and Chen, Y., 2017, "Porous Structure Fabrication Using a Stereolithography-Based Sugar Foaming Method," ASME J. Manuf. Sci. Eng., **139**(3), p. 031015.
[10] Hwa, L. C., Rajoo, S., Noor, A. M., Ahmad, N., and Uday, M., 2017, "Recent Advances in 3D Printing of Porous Ceramics: A Review," Curr. Opin. Solid State Mater. Sci., **21**(6), pp. 323–347.
[11] Zhang, Q., Zhang, F., Medarametla, S. P., Li, H., Zhou, C., and Lin, D., 2016, "3D Printing of Graphene Aerogels," Small, **12**(13), pp. 1702–1708.
[12] M'barki, A., Bocquet, L., and Stevenson, A., 2017, "Linking Rheology and Printability for Dense and Strong Ceramics by Direct Ink Writing," Sci. Rep., **7**(1), pp. 1–10.
[13] Li, V. C.-F., Dunn, C. K., Zhang, Z., Deng, Y., and Qi, H. J., 2017, "Direct Ink Write (DIW) 3D Printed Cellulose Nanocrystal Aerogel Structures," Sci. Rep., **7**(1), pp. 1–8.
[14] Guo, Z., Yang, R., Wang, T., An, L., Ren, S., and Zhou, C., 2021, "Cost-Effective Additive Manufacturing of Ambient Pressure-Dried Silica Aerogel," ASME J. Manuf. Sci. Eng., **143**(1), p. 011011.
[15] Hu, F., Wu, S., and Sun, Y., 2019, "Hollow-Structured Materials for Thermal Insulation," Adv. Mater., **31**(38), p. 1801001.
[16] Hu, L., Wang, C.-A., and Huang, Y., 2011, "Porous YSZ Ceramics With Unidirectionally Aligned Pore Channel Structure: Lowering Thermal Conductivity by Silica Aerogels Impregnation," J. Eur. Ceram. Soc., **31**(15), pp. 2915–2922.
[17] Sun, Z., Lu, C., Fan, J., and Yuan, F., 2016, "Porous Silica Ceramics With Closed-Cell Structure Prepared by Inactive Hollow Spheres for Heat Insulation," J. Alloys Compd., **662**, pp. 157–164.
[18] Østergaard, M. B., Cai, B., Petersen, R. R., König, J., Lee, P. D., and Yue, Y., 2019, "Impact of Pore Structure on the Thermal Conductivity of Glass Foams," Mater. Lett., **250**, pp. 72–74.
[19] Reichenauer, G., Heinemann, U., and Ebert, H.-P., 2007, "Relationship Between Pore Size and the Gas Pressure Dependence of the Gaseous Thermal Conductivity," Colloids Surf., A, **300**(1–2), pp. 204–210.
[20] Román-Manso, B., Muth, J., Gibson, L. J., Ruettinger, W., and Lewis, J. A., 2021, "Hierarchically Porous Ceramics via Direct Writing of Binary Colloidal Gel Foams," ACS Appl. Mater. Interfaces, **13**(7), pp. 8976–8984.
[21] Muth, J. T., Dixon, P. G., Woish, L., Gibson, L. J., and Lewis, J. A., 2017, "Architected Cellular Ceramics With Tailored Stiffness via Direct Foam Writing," Proc. Natl. Acad. Sci. U. S. A., **114**(8), pp. 1832–1837.
[22] Huang, K., Elsayed, H., Franchin, G., and Colombo, P., 2020, "3D Printing of Polymer-Derived SiOC With Hierarchical and Tunable Porosity," Addit. Manuf., **36**, p. 101549.
[23] Chan, S. S., Sesso, M. L., and Franks, G. V., 2020, "Direct Ink Writing of Hierarchical Porous Alumina-Stabilized Emulsions: Rheology and Printability," J. Am. Ceram. Soc., **103**(10), pp. 5554–5566.
[24] Minas, C., Carnelli, D., Tervoort, E., and Studart, A. R., 2016, "3D Printing of Emulsions and Foams Into Hierarchical Porous Ceramics," Adv. Mater., **28**(45), pp. 9993–9999.
[25] Seitz, H., Deisinger, U., Leukers, B., Detsch, R., and Ziegler, G., 2009, "Different Calcium Phosphate Granules for 3-D Printing of Bone Tissue Engineering Scaffolds," Adv. Eng. Mater., **11**(5), pp. B41–B46.
[26] An, L., Wang, J., Petit, D., Armstrong, J. N., Hanson, K., Hamilton, J., Souza, M., Zhao, D., Li, C., and Liu, Y., 2020, "An all-Ceramic, Anisotropic, and Flexible Aerogel Insulation Material," Nano Lett., **20**(5), pp. 3828–3835.
[27] Franchin, G., Scanferla, P., Zeffiro, L., Elsayed, H., Baliello, A., Giacomello, G., Pasetto, M., and Colombo, P., 2017, "Direct Ink Writing of Geopolymeric Inks," J. Eur. Ceram. Soc., **37**(6), pp. 2481–2489.
[28] Kim, F., Kwon, B., Eom, Y., Lee, J. E., Park, S., Jo, S., Park, S. H., Kim, B.-S., Im, H. J., and Lee, M. H., 2018, "3D Printing of Shape-Conformable Thermoelectric Materials Using all-Inorganic Bi 2 Te 3-Based Inks," Nat. Energy, **3**(4), pp. 301–309.
[29] Tang, S., Yang, L., Li, G., Liu, X., and Fan, Z., 2019, "3D Printing of Highly-Loaded Slurries via Layered Extrusion Forming: Parameters Optimization and Control," Addit. Manuf., **28**, pp. 546–553.
[30] Wei, T. S., Ahn, B. Y., Grotto, J., and Lewis, J. A., 2018, "3D Printing of Customized Li-Ion Batteries With Thick Electrodes," Adv. Mater., **30**(16), p. 1703027.
[31] Comminal, R., Serdeczny, M. P., Pedersen, D. B., and Spangenberg, J., 2019, "Motion Planning and Numerical Simulation of Material Deposition at Corners in Extrusion Additive Manufacturing," Addit. Manuf., **29**, p. 100753.
[32] Hwang, S.-W., Jung, H.-H., Hyun, S.-H., and Ahn, Y.-S., 2007, "Effective Preparation of Crack-Free Silica Aerogels via Ambient Drying," J. Sol-Gel Sci. Technol., **41**(2), pp. 139–146.
[33] Treuel, L., Eslahian, K., Docter, D., Lang, T., Zellner, R., Nienhaus, K., Nienhaus, G., Stauber, R., and Maskos, M., 2014, "Physicochemical Characterization of Nanoparticles and Their Behavior in the Biological Environment," Phys. Chem. Chem. Phys., **16**(29), pp. 15053–15067.
[34] Liu, W., Yang, X., Zhang, Y., Xu, M., and Chen, H., 2014, "Ultra-stable Two-Dimensional MoS 2 Solution for Highly Efficient Organic Solar Cells," RSC Adv., **4**(62), pp. 32744–32748.
[35] Zhang, S., Lan, Q., Liu, Q., Xu, J., and Sun, D., 2008, "Aqueous Foams Stabilized by Laponite and CTAB," Colloids Surf., A, **317**(1–3), pp. 406–413.
[36] Hao, N., Chen, X., Jayawardana, K. W., Wu, B., Sundhoro, M., and Yan, M., 2016, "Shape Control of Mesoporous Silica Nanomaterials Templated With Dual Cationic Surfactants and Their Antibacterial Activities," Biomater. Sci., **4**(1), pp. 87–91.